Environ Fluid Mech (2012) 12:185–200
DOI 10.1007/s10652-011-9226-z

ORIGINAL ARTICLE

Evaluation of numerical simulations of CO_2 transport in a city block with field measurements

Andres Gartmann · Mathias D. Müller · Eberhard Parlow · Roland Vogt

Received: 31 December 2010 / Accepted: 20 September 2011 / Published online: 29 October 2011

Abstract Studying urban air-transport phenomena is highly complex, because of the heterogenous flow patterns that can arise. The main reason for these is the variable topology of urban areas, however, there is a large number of influencing variables such as meteorological conditions (e.g., wind situation, temperature) and anthropogenic factors such as traffic emissions. During a one-year CO_2 measurement campaign in the city of Basel, Switzerland, steep CO_2 gradients were measured around a large building. The concentration differences showed a strong dependency on the local flow regimes. Analysis of the field data alone did not provide a complete explanation for the mechanisms underlying the observed phenomena. The key numerical parameters were defined and the influence of turbulent kinetic energy dependency on the time interval for the Reynolds decomposition was studied. A Reynolds-Average Navier-Stokes Computational Fluid Dynamics (CFD) approach was applied in the study area and the CO_2 concentrations were simulated for six significant meteorological situations and compared to the measured data. Two flow regimes dependent on the wind situation, which either enhanced or suppressed the concentration of CO_2 in the street canyon, were identified. The enhancement of CO_2 in the street canyon led to a large difference in CO_2 concentration between the backyard- and street-sides of a building forming the one wall of the canyon. The specific characteristics of the flow patterns led to the identification of the processes determining the observed differences in CO_2 concentrations. The combined analysis of measurement and modeling showed the importance of reliable field measurements and CFD simulations with a high spatial resolution to assess transport mechanisms in urban areas.

Keywords CFD · CO_2 transport · Urban areas · Turbulent kinetic energy · RANS

A. Gartmann (✉) · M. D. Müller · E. Parlow · R. Vogt
Institute of Meteorology, Climatology and Remote Sensing, University of Basel,
Klingelbergstrasse 27, 4056 Basel, Switzerland
e-mail: andres.gartmann@unibas.ch

1 Introduction

Human activity in urban areas degrades air quality, which in turn strongly affects the quality of life and health of the population. Understanding the transport mechanisms of anthropogenic emissions from fossil-fuel combustion in urban areas is a key issue in assessing the impact of pollution and improving air quality. Heterogeneous flow patterns evolve in both space and time owing to the complexity of the topology in urban areas. The dispersion of pollutants is dominated by micro-scale wind patterns within the urban boundary layer [13]. The flow patterns lead to strong horizontal concentration gradients of air pollutants, greenhouse gases and particles [28]. CO_2 concentration can be measured and can be used as a substitute for combustion emissions, such as from traffic, in urban areas. Further assessment of the contribution to the global CO_2 cycle of the urban sources is challenging, as spatially significant measurement data in urban areas are difficult to obtain [9].

A better understanding of such air borne phenomena and the key mechanisms for the dispersion of pollutants in urban areas can be gained by different approaches.

Experimental studies with simple objects and numerical simulations such as data from wind-tunnel experiments have been used to evaluate numerical methods for turbulent simulations, such as Large Eddy Simulations (LES) or turbulent Reynolds-Average Navier-Stokes (RANS) models [7,15,4,6]. These methods help to develop and verify numerical models but the simplification of the geometry and the idealized flow conditions in experimental setups do not have the same relevance to real situations as do field measurements. Extensive field campaigns [9,20,28] provide data from point measurements that have high temporal resolution, but contain little information about the spatial properties of the flow. Finally, model studies with idealized city geometries have been utilized to study urban air-borne phenomena [12,21,1,27,11]. An overview of street canyon modeling is given by [24]. Numerical methods, such as computational fluid dynamics (CFD), are well-known instruments for computing and analyzing flow patterns [13]. Different studies have been conducted with idealized geometries and air pollution transport, [23], but only a few numerical studies used complex city geometries and field-measurement data to validate the numerical results [10, 29].

To capture transport dynamics of CO_2 distribution in a street canyon, a previous study measured CO_2 concentrations in a street canyon in Basel, Switzerland, and in an adjacent backyard. The result showed a large difference in CO_2 concentration between the front (street-side) and back of a large building that constituted part of the canyon wall. The CO_2 concentration differences were strongly dependent on wind direction and only weakly dependent on traffic frequency and atmospheric stability [26].

This article describes the numerical approach and the comparison of CFD CO_2 results with field measurement data in a real city geometry. Basic guideline exists for CFD calculations in urban areas, e.g., [8] or [22]. Based on these guidelines, a sensitivity study was first conducted to determine the numerical parameters that influence the calculations. An appropriate time-average period for the Reynolds decomposition in the measurement data had to be defined for the comparison of RANS models with field measurements. This was achieved in other studies by minimizing the error between modelled and measured data through reducing the length of the Reynolds decomposition time-average period, e.g., [5]. The length of the Reynolds decomposition time-average period has a significant influence on the turbulent kinetic energy (TKE) in street canyons. The influence of time-average periods on the velocity and turbulence profiles in a street canyon was analyzed in detail using field data of the Basel Urban Boundary Experiment (BUBBLE) [20].

Six representative wind flow conditions were modeled with the results from the sensitivity analysis and the CO_2 field-measurement data analysis. These were compared to the measurement data to study the mechanisms in detail and to address the reason for the strong dependency of the CO_2 concentration differences on wind condition.

This article shows the application of CFD in a complex city geometry and the comparison to field measurements, whereby the ability of CFD methods to obtain flow characteristics and transport phenomena of fluid components within real urban areas was shown. Further, it shows the influence of, and gives recommendations for, the definition of the time-average period for the Reynolds decomposition of the field measurements in comparison to RANS results.

2 Methods

2.1 Measurements

Two measurement data sets used for this study were obtained at two sites in the city of Basel, Switzerland. Figure 1 shows the center of Basel with the locations of the two sites (A,B).

2.1.1 Sensitivity analysis

Field-measurement data of the Basel Urban Boundary Experiment (BUBBLE) [20] were used for the sensitivity analysis. During the one year BUBBLE campaign, a measurement tower was located within a street canyon in a densely built-up area of the city of Basel, Fig. 1a. Wind fields were measured on six levels using sonic anemometers with a time resolution of 20 Hz. This measurement setup provides an ideal framework to evaluate the performance of solvers and numerical parameters for CFD calculations in a complex topology.

Fig. 1 Location of the two study sites in Basel, Switzerland. *A* indicates the computational domain for the sensitivity analysis. *B* the location for the CO_2 transport simulations. The green shaded area in *B* indicates the building shown in Fig. 2. Base map copyright GVA BS, 25102002

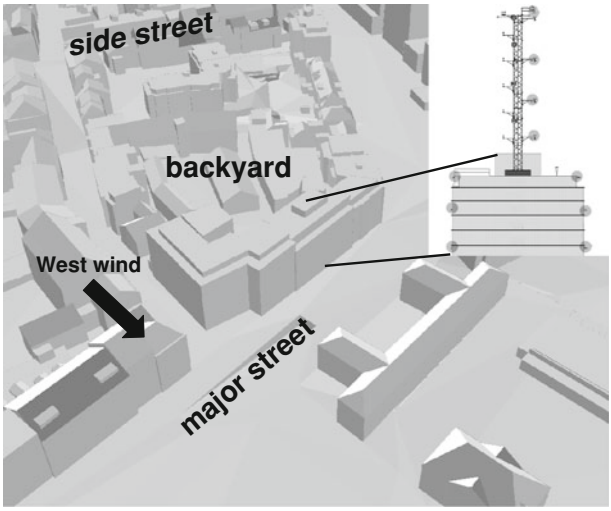

Fig. 2 Schematic view over the measurement site and cross section through the measurement setup (adapted from [26])

2.1.2 CO_2 *dispersion*

Figure 2 shows the area and the large 20 m high building (indicated as site B in Fig. 1), located in the center of Basel, Switzerland, as a computer-aided design (CAD) model. A main street with North-South orientation and heavy traffic runs in front of the building and at the rear of the building there is a large backyard surrounded by smaller buildings. CO_2 measurements were carried out around the building from September, 2004 to August, 2005. A closed-path gas analyzer (Li6262, LiCOR) and a multiplexer system with 10 inlets were used to measure the CO_2 concentration at 4, 15 and 21 m above the ground on each side and at 25, 28.5, 34 and 40 m over the top of the building on a measurement tower.

The concentration profiles were averaged over 30 min intervals. The detailed configuration can be seen in the schematic view, where the dots represent the inlets for the CO_2 measurements, inset Fig. 2. The stationary measurement tower on top of the building was also equipped with an eddy covariance system. The streets adjoining the other side of the smaller buildings are sidestreets with less traffic. The two dominant wind directions over the region are from West, indicated by the arrow, and East [20].

2.2 Numerical modeling

2.2.1 Governing equations

The turbulent wind field in urban areas are strongly influenced by the heterogeneity of the topology. For this reason, stability has a minor influence within the lower urban boundary layer [14]. This allows the simplification of neglecting buoyancy and thermal effects, which is applicable for advection dominant flows. Following [25], the Navier-Stokes equations (NSE) for incompressible fluid flow can be written as:

$$\frac{DU_i}{Dt} = -\frac{1}{\rho}\frac{\delta p}{\delta x_i} + f_i + \mu\frac{\delta^2 U_i}{\delta x_j^2} \tag{1}$$

where U_i are the velocity components in three dimensions, ρ the density, f_i body forces, p the pressure and μ the viscosity of the fluid [25]. Together with the incompressible continuity equation

$$\frac{\delta U_i}{\delta x_i} = 0 \tag{2}$$

the NSE build the governing equations for CFD simulations. By applying the Reynolds decomposition

$$U_i = \langle U_i \rangle + u_i \tag{3}$$

on the NSE, Eq. 1, one of the most applied turbulent model approaches, the Reynolds-Averaged Navier-Stokes (RANS), Eq. 4, is obtained [18].

$$\frac{\bar{D}\langle U_i \rangle}{\bar{D}t} = -\frac{1}{\rho}\frac{\delta \langle p \rangle}{\delta x_i} + f_i + \nu \frac{\delta^2 \langle U_i \rangle}{x_i^2} - \frac{\delta \langle u_i u_j \rangle}{\delta x_j} \tag{4}$$

where ν is the kinematic viscosity $\nu = \mu/\rho$. The additional terms $\frac{\delta \langle u_i u_j \rangle}{\delta x_j}$ are the Reynolds stresses and increase the number of unknown variables to more than four. The Reynolds stresses have to be obtained by other assumptions, which is called the closure problem [18].

One way to solve the closure problem is through models using the viscosity hypothesis [18]. The turbulent-viscosity hypothesis introduces a proportional relation between the Reynolds stresses and the mean rate of strain using a scalar coefficient, the turbulent viscosity ν_t

$$\langle u_i u_j \rangle = \frac{2}{3} k \delta_{ij} - \nu_t \left(\frac{\delta \langle U_i \rangle}{\langle x_j \rangle} + \frac{\delta \langle U_j \rangle}{\langle x_i \rangle} \right) \tag{5}$$

where k is the turbulent kinetic energy. Two-equation models, where the $k - \epsilon$ model is one of the most applied approaches, solve for the TKE k and the dissipation ϵ each an additional transport quation [18]. Thus, the turbulent viscosity can be obtained from:

$$\nu_t = C_\mu \frac{k^2}{\epsilon} \tag{6}$$

where $C_\mu = 0.09$ is a model constant [18]. A good overview of other two-equation approaches can be found in [16].

A multicomponent flow approach was used for the simulation of the CO_2 dispersion. In multicomponent simulations the fields are computed only for a single fluid based on the governing equations. The fluid is considered as a mixture of single fluids in order to incorporate the influence of the different fluid components. The properties of the mixture in each cell is dependent on the proportion of each component in the cell. The proportion of each component in the domain can be calculated using a separate continuity equation for each component k:

$$\frac{D\tilde{\rho_k}}{Dt} = \frac{\delta \tilde{\rho_k}}{\delta t} + \frac{\delta(\tilde{\rho_k}\tilde{U_i})}{\delta x_i} = -\frac{\delta}{\delta x_i}\left\{ \rho_k (\tilde{U_{ki}} - \tilde{U_i}) - \overline{\rho_k u_i} \right\} \tag{7}$$

where $\sim$ indicates the mass-average and $\tilde{U_{ki}}$ the mass-averaged velocity of the fluid of component k [2]. The relative mass flux term $(\tilde{U_{ki}} - \tilde{U_i})$ models the motions of the single components in the mixture. The primary effect for these motions are the concentration gradients, which lead to relative motions in form of diffusion of the components in the mixture. The physical influence of the component is incorporated using the kinematic diffusivity D_k.

The turbulent fluxes $\overline{\rho_k u_i}$ can be modeled using the eddy dissipation-assumption, which leads to a advection-diffusion equation for the fraction Y_k:

$$\frac{\delta(\bar{\rho}\tilde{Y}_k)}{\delta t} + \frac{\delta(\bar{\rho}\tilde{U}_i\tilde{Y}_k)}{\delta x_i} = \frac{\partial}{\partial x_i}\left\{\frac{\partial Y_k}{\partial x_i}\left(\rho_k D_k + \frac{\mu_t}{Sc_t}\right)\right\} \tag{8}$$

where Sc_t is the turbulent Schmidt number $Sc = \nu_t/D$. If all continuity equations (Eq. 7) are summed, the standard continuity equation can be obtained (Eq. 2).

2.2.2 Setup

The commercial software package ANSYS CFX [2] was used for all CFD calculations. The buildings within 150 m of the CO_2 measurement location were included in the CFD computations. The meshes were constructed with the package ANSYS ICEM CFD [3]. All numerical simulations were steady-state simulations.

For the ground and building walls, smooth wall-functions were applied because the roughness influence would be of a smaller order than the resolved scales and a slip condition was set for the top of the domain, which ensured a parallel flow at the top of the boundary [8].

The CO_2 dispersion was modeled using a multicomponent approach. The simulated mixture was given the gaseous fluid properties of air, CO_2 and N_2 as a constraint. The mass fraction of air and CO_2 is computed according Eq. 8, with the mass fraction of N_2 as residual to ensure unity in every cell. The influence of the CO_2 traffic source was modeled as a surface source term with constant fluxes from the streets. Different source strengths had to be defined, because of the irregular traffic frequency on the main street (average 800–1200 vehicles per hour) compared to the smaller streets ($<$ 400 vehicles per hour). For weekend situations, the source strengths on the streets were reduced by half, due to lower traffic density. Six conditions were modeled (three westerly wind and three easterly wind situations) for the comparison and the analysis of the experimentally determined CO_2 characteristics. The numerical parameters as mesh resolution, boundary conditions and turbulence closure for the CO_2 CFD calculations were defined based on the results of a prior sensitivity analysis.

2.3 Sensitivity analysis

The influence of the numerical parameters of the applied CFD code was evaluated because the evaluation of CFD calculations should be based on high resolution measurements [17]. The domain for the validation cases had a spatial extent over 200 m in both horizontal directions within a densely built-up area. The vertical extent was 80 m and the maximal height of the buildings in the model domain approx. 20 m.

The following numerical parameters were tested with the applied numerical CFD code: (1) mesh, (2) turbulence model, (3) boundary condition, based on the general guidelines for urban CFD calculations [8,22]. All results were compared to the mean velocity and the TKE measurement profiles to obtain their performance.

1—Mesh: Four meshing methods with different complexities were tested using cell-size resolutions between 0.8 m and 4 m: (A) Plain tetrahedral, (B) tetrahedral with prism layers around walls, (C) tetrahedral with prism layers around walls and hexahedral shapes in the free stream regions, (D) cartesian [3].

The advantage of tetrahedral meshes (A, B, C) is their ability to represent the geometrical data more or less independently of the resolution [25]. Although dependent on mesh resolution, Cartesian meshes (D) result in simplification of the geometrical data. Tetrahedral

meshes can produce elements with poor aspect ratios [22]. Changing distances of the first mid-point to surface elements can be prevented in (B) by adding prism layers near surfaces. Hexahedral element shapes introduce smaller errors and have a better iteration convergence [8], which was tested by adding hexahedral, rectangular shapes in the free stream region (C).

The plain tetrahedral meshes show poor results near walls because of the changing distances of the element midpoints to the wall surfaces. This leads to changes in the y^+ value (dimensionless distance from the wall), which is a key value for the necessary wall-functions [2]. The strongest correlation with the measured profiles was achieved using a minimum of three prism cell layers around walls. The additional hexahedral elements in the free stream regions had a minor influence on the results and only small effects on the divergence properties of the computations. In contrast to the tetrahedral meshes, the Cartesian meshes rendered poor results for the wind patterns within the street canyon.

The best results were found using tetrahedral meshes with approximately 1 m resolution and a minimum of three prismatic layers around walls.

2—Turbulence Model: Both the standard $k-\epsilon$ model and the RNG $k-\epsilon$ model were tested, because the widely used $k-\epsilon$ turbulence closure for RANS calculation has limitations due to the overproduction of kinetic energy in regions with stagnated flow situations [8]. However, the direct comparison of computations using the RNG $k-\epsilon$ approach and the standard model, showed no significant difference in this case.

3—Boundary Conditions: Uniform inlet conditions as well as logarithmic profiles were tested. For the logarithmic inlet profiles of the mean velocity $U(z)$ Eq. 9, as suggested by [19], was applied in combination with the friction velocity U_{fric}

$$U(z) = \frac{U^*_{fric}}{\kappa} \cdot \ln\left(\frac{z+z_0}{z_0}\right) \tag{9}$$

$$U^*_{fric} = \frac{\kappa \cdot U_h}{\ln\left(\frac{h+z_0}{z_0}\right)} \tag{10}$$

The reference mean velocity U_h is the velocity at a reference altitude over ground h, z the vertical distance, z_0 is the roughness length and κ the von Karman constant. For the sensitivity analysis, the reference height to calculate the friction velocity U^*_{fric}, the height above ground of the highest measurement point was used ($h = 32\,\text{m}$).

For the TKE k and the dissipation ϵ, two approaches were tested: (A) as suggested by [19] a constant TKE value k is derived from the friction velocity

$$k = \frac{U^{*2}_{fric}}{\sqrt{C_\mu}} \tag{11}$$

where C_μ is the model constant for the k- ϵ model ($C_\mu = 0.09$) and the dissipation ϵ is computed according:

$$\epsilon = \frac{U^{*2}_{fric}}{\kappa \cdot (z+z_0)} \tag{12}$$

The second approach (B) relates k to the turbulence intensity I and the mean velocity U:

$$k = \frac{3}{2} \cdot U^2(z) \cdot I^2 \tag{13}$$

and also dissipation:

$$\epsilon = \frac{k^{\frac{3}{2}}}{L_t} \tag{14}$$

where L_t is a characteristic length scale. Following [18] and [2] the vertical extension of the domain of 80 m was used.

3 Results and discussion

The time-average period for the Reynolds decomposition of the measured data had to be specified before the field measurements could be compared to velocities from RANS models.

3.1 Time-average period

Figure 3a shows the correlation between measured mean velocity V_{mean} and the TKE values for time-average periods of 1200 s and (b) 30 s for the same data set of July and August, 2002 in the street canyon, where the sensitivity analysis was conducted.

A strong dependency between time-average periods used for the Reynolds decomposition and the TKE values in the street canyon was observed. The ratio between the mean velocity and the TKE was significantly higher when longer time-averages (e.g., 1200 s) were applied compared to shorter time-averages (e.g., 30 s). This indicates that different time-averages lead to different ratios between the mean velocity and TKE. This is an important fact when RANS results are compared to measurement data, which is discussed in the next section.

Figure 4 shows the profiles for measured data with different time-average periods and the numerical results from the sensitivity analysis. The mean velocity values are only weakly influenced by the time-average periods, as can be seen in Fig. 4a. Figure 4b shows the influence of the time-average periods on the TKE distribution within the street canyon and the mean deviation, where the time-average period has a significant influence on the TKE profiles. For the mean velocity components, a good agreement between observations and model results was achieved, as can be seen in Fig. 4a. Using approach (A) for the turbulence entities leads to TKE profiles with higher TKE than with approach (B), Fig. 4b.

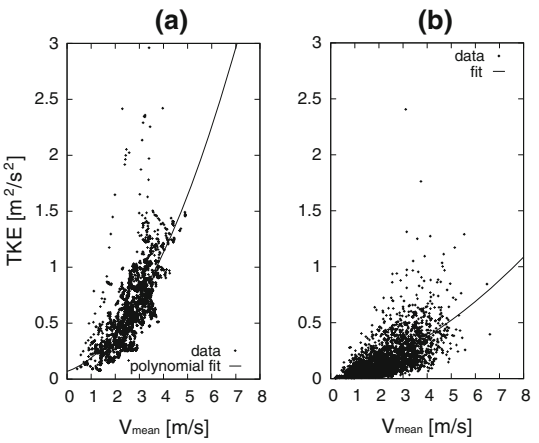

Fig. 3 Data points (+) represent the turbulent kinetic energy (TKE) magnitude at top of the tower (32 m above ground) and the *solid lines* represent the polynomial fit for Reynolds decomposition time-average periods of **a** 1200 s, **b** 30 s for SE wind angle (130°)

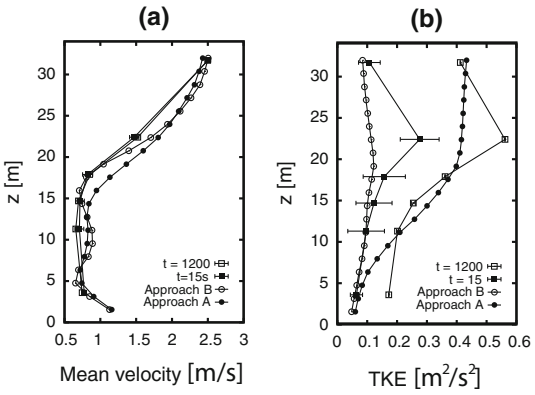

Fig. 4 Comparison between modeled data using Eqs. 11 and 12 (Approach A) or based on Eqs. 13 and 14 (Approach B) and measured data (time-average period for Reynolds decomposition 1200 and 30 s): **a** mean velocity, **b** TKE as profile from distance to the ground $z[m]$

A weak correlation could be found in the mean velocity profiles, using the approach with constant inlet turbulent values (A). Constant boundary conditions for TKE lead to comparable results for time-average periods of >600 s, but then to weaker correlations with mean velocity values, see Fig. 4. The best results were found with the boundary conditions (B) for the TKE ($I = 5-10\,\%$) together with time-average period of 15–60 s for all studied conditions and over all six measured levels in the street canyon. The results are in good agreement with appropriate time-average periods described in another study [5]. The better accordance between the CFD results and the measurements on all six levels using over two months of 20 Hz measurement data for the analysis indicated that there is an optimal average-time period for comparison. Other studies found the same appropriate time-average periods. Therefore, the use of 15–60 s for the Reynolds decomposition of field measurements in street canyons can be recommended for the comparison to RANS results. Because a defined time-average period does not exist for the Reynolds decomposition in RANS models caused by the model assumptions, the time-average period is not to be considered as the time-scale for the TKE. Generally, long time-average periods are associated with large spatial scale eddies. It is possible that, owing to the high spatial resolution in the model, explicitly resolved turbulence (as advection in the CFD results) is accounted as TKE in measurements. Further, an assumption for the Reynolds decomposition is the statistical stationarity of the flow. In urban areas the stationary condition for the Reynolds decomposition is rarely fulfilled and the longer the time-average length is, the higher the probability that the assumption is not fulfilled.

Independent of the time-average period, the significant change in the TKE profile at roof level (approx. 20 m above ground) has a poorer correlation with the measurement data compared to the lower part of the canyon, Fig. 4. Neither of the applied models were able to adequately simulate the acceleration of the TKE. This might be due to either the model formulation or the limitation of an insufficient horizontal extent. No significant differences could be found by comparing simple uniform inlet conditions and logarithmic profiles, because the influence of the topology was significantly stronger than the influence of the boundary conditions in densely built-up areas. Nevertheless the logarithmic profiles are recommended.

3.2 CO_2 concentration simulations

The measured CO_2 concentrations showed large differences between the street and backyard profiles, with a strong dependency on wind direction [26]. During westerly wind flow, the

Table 1 30 min averaged velocity U_{mag} and background concentrations $c_{\mathrm{background}}$ measured at top of the tower during the six scenarios. Day stands for weekdays (WD) and weekends (WE) and the absolute wind direction (WDir)

nr	Day	Date	WDir	U_{mag}	$c_{\mathrm{background}}$
1	WE	03.07.2005–09:00	Easterly	1.38	408.7
2	WE	17.07.2005–11:30	Westerly	1.82	378.6
3	WE	23.07.2005–09:00	Easterly	1.75	401.3
4	WE	23.07.2005–11:00	Westerly	2.4	370.2
5	WD	28.07.2005–12:00	Easterly	3.11	383.5
6	WD	21.07.2005–10:30	Westerly	3.55	378.4

Table 2 Measurement and modeled differences between front and backyard CO_2 concentrations for weekdays (WD) and weekends (WE) for easterly and westerly wind situations at the six conditions

nr	Day	WDir	λ_{meas} [−]	λ_{cfd} [−]	η []
1	WE	Easterly	5.4	6.7	0.24
2	WE	Westerly	32.2	66.7	1.07
3	WE	Easterly	13.3	16.1	0.21
4	WE	Westerly	51.3	49.3	0.04
5	WD	Easterly	6.9	4.5	0.34
6	WD	Westerly	52.7	66.9	0.27

CO_2 concentration was much higher on the street side then on the rear side of the building. The concentration differences between the two sides of the building were negligible during easterly wind episodes. There was practically no dependency on stability conditions and only a weak dependency on traffic frequency. To involve the representative cases for one week, 3 days were modeled: one weekday, Saturday and Sunday. A westerly and an easterly wind case was included for each weekday type. To account for different velocities for each of the three westerly and easterly wind cases, different velocities based on the measurement point on top of the tower on the building were selected in the data. As discussed, the time-average period had a strong influence on the TKE distribution in a street canyon. As the averaging interval of the concentration profiles was at least 30 min, boundary conditions suggested by [19] were used and the average mean velocities of 30 min at top of the tower for the six situations were used as U_h in Eq. 10. Table 1 summarizes the six situations with the 30 min averaged velocities and the CO_2 concentration, which were used as background concentrations measured at top of the tower at 40 m above ground.

To compare the measured and the modeled results qualitatively, the concentrations on each side of the building are summed with the highest available temporal resolution of 30 min and then the difference λ between the front and backyard side were calculated according:

$$\lambda = \sum c_{i,front} - \sum c_{i,back} \tag{15}$$

where c_i expresses the concentration at 4, 15, respectivly 21 m above ground. Table 2 shows the concentration differences λ based on the measurements and the CFD computations. The relative error η was computed using:

$$\eta = \left| \frac{\lambda_{cfd} - \lambda_{meas}}{\lambda_{meas}} \right| \tag{16}$$

As can be seen in Table 2, a good correlation was found between the modeled results and the experimental data (relative error <30%). The variable dispersion of the CO_2 from the street to the measurement points (Fig. 2) were the main reason for the strong dependency of

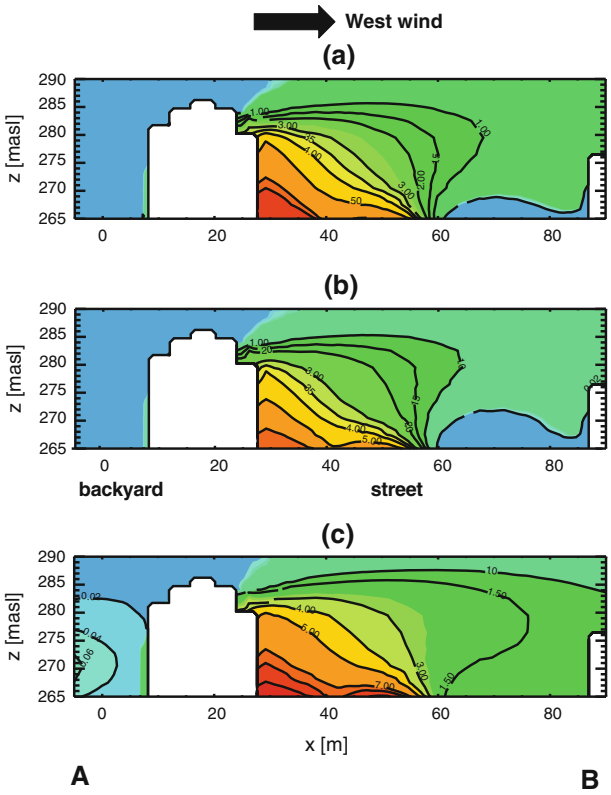

Fig. 5 Contour plot (location indicated in Fig. 8) of percentage of CO_2 relative to background concentration during westerly situations (Table 1) with following velocity magnitudes: **a** situation 2—$U_{mag} = 1.8$ m/s; **b** situation 4—$U_{mag} = 2.4$ ms^{-1}; **c** situation 6—$U_{mag} = 3.6$ m/s

the concentration differences between backyard and street. The good correlation between the measured and modeled differences of the CO_2 concentrations leads to the conclusion that the main characteristics of the flow patterns in the street canyon could be modeled in sufficient detail. The outlier on the weekend during the westerly wind episode might be due to higher traffic frequency or local irregular high emissions and could not be completely explained over that time period.

One of the advantages of CFD calculation is their spatial validity. The flow and corresponding CO_2 part in the fluid can be visualized and analyzed by using the CFD data.

The levels of the CO_2 layers could be visualized using the cross sections of the CO_2 mass part fields, representing the CO_2 concentrations. Figure 2 shows an overview of the site and Fig. 8 the location of the cross sections. Figure 5 shows the relative CO_2 concentration during westerly wind situations. The CO_2 from the street was transported towards the building wall in all three cases. A significantly higher CO_2 concentration (averaged 5 %) occurred on the western side of the street canyon (Fig. 5), whereas approximately the background CO_2 concentration was found on the eastern side.

One can see that the higher the velocity was, the more of the emitted CO_2 from the street was transported to the right area. Figure 6 shows the concentration levels during easterly wind situations, where a completely different CO_2 distribution was found. The CO_2 emitted from

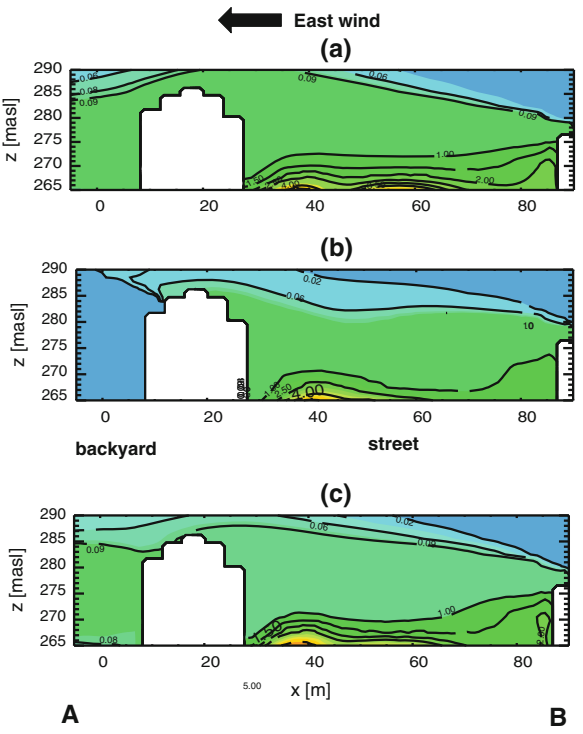

Fig. 6 Contour plot of relative CO_2 concentration (% of background) during easterly situations with following velocities: **a** situation 1—$U_{mag} = 1.4$ m/s; **b** situation 3—$U_{mag} = 1.8$ m/s; **c** situation 5—$U_{mag} = 3.1$ m/s

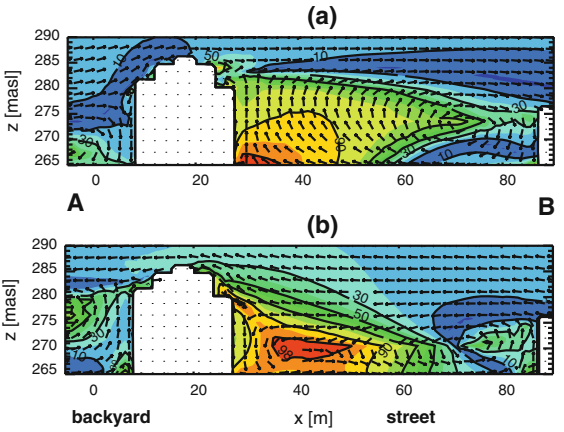

Fig. 7 Vector and contour plot: **a** westerly wind situation (Table 2—nr. 6) **b** easterly wind situation (Table 2—nr. 5). Contours describe magnitude of the velocity component normal to the plane shown in percentage

the street was not transported vertically, but concentrated close to the street level. Concentrations not higher than 1 % of the background can be expected near the left side of the street canyon. For all velocities, the CO_2 concentration field was more or less homogeneous in the area directly above the street. The cause of the concentration levels lies in the structure of the evolving flow patterns in the street canyon. Figure 7a shows a vector plot during westerly wind episodes, where the vectors show the projected velocity components on the cross section and the contour lines the percentage of the velocity magnitude of the components normal to the plane, Fig. 8. Figure 8 shows the three dimensional extent of the flow 5 m above the

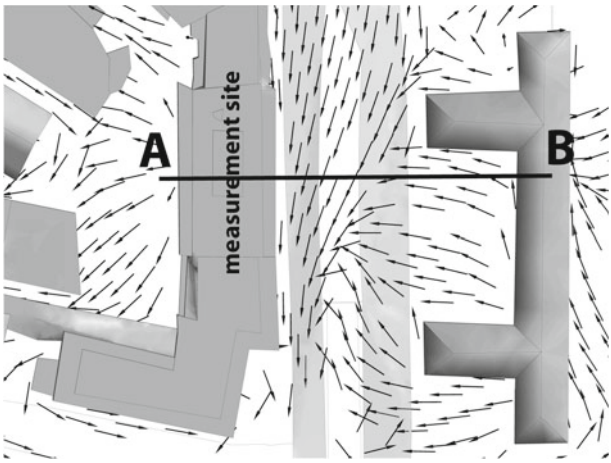

Fig. 8 Vector plot during westerly wind episode

ground and with A and B indicating the cross section showed in Fig. 5, 6, and 7, to explain the influence of the velocity components parallel to the street.

One vortex, rotating clockwise, was developed with a center point near the eastern building of the street canyon during westerly wind episodes, Fig. 7a. The flow near the ground had components orthogonal to the building wall on the left side, resulting in emitted CO_2 being transported towards the building wall. One prolate vortex was developed with the center point on the same height above the ground during easterly wind episodes, Fig. 7b. This counter-clock wise rotation transported the street CO_2 away from the building wall on the west side of the street.

Velocities evolved parallel to the building wall in the street canyon in both easterly and westerly wind episodes. As a result, the emitted CO_2 from the street was transported and concentrated along the street. CO_2 was transported to the measurement points by the combination of the velocity components vertical to the building wall, due to the vortex structures, and the components along the street.

Turbulence intensity is a measure of the ratio between the TKE and the mean velocity. By solving Eq. 13 to I (intensity), the turbulence intensity distribution over the street canyon can be visualized (Fig. 9). A higher intensity was found on the right side of the street canyon and lower intensity near the right building wall during westerly and easterly wind episodes. This indicates, that the TKE drove dispersion on the right side of the canyon, while the TKE had a lower impact on the CO_2 distribution near the measurement points on the left building wall. This supports the homogeneous CO_2 distribution during easterly wind episodes, where TKE counteracted to the transport effect of the counter-clockwise rotating vortexes. During westerly wind episodes the low turbulence intensity near the left building wall supported the acceleration of the CO_2.

The flow patterns are summarized schematically in Fig. 10. The dots on the left building wall indicate the points where the CO_2 measurements were made.

The separation line of the flow is defined by the height of the larger building (left side of the street canyon) during westerly wind situations. During easterly wind episodes, the separation line between the two flow patterns is defined by the level of the lower building (Fig. 10a). These two opposite vortex structures were the cause of the strong dependency of the CO_2 concentrations on the wind situations. The high mean velocity over the main street visible in Fig. 8 and indicated in the contours in Fig. 7 supported the accumulation of CO_2

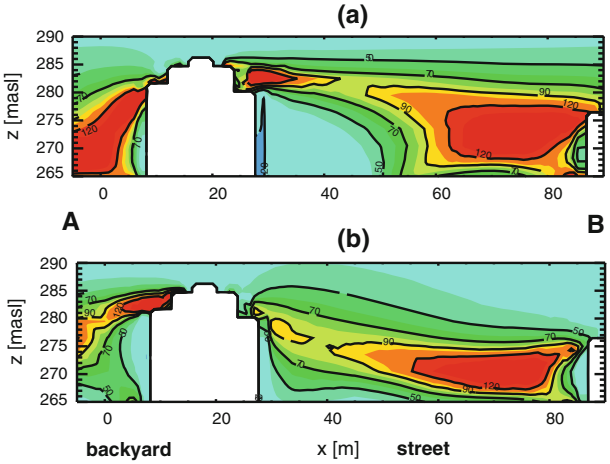

Fig. 9 Vector and contour plot with **a** westerly wind (Table 2—nr. 6), **b** easterly wind (Table 2—nr. 5). Contours describe turbulence intensity (Eq. 13)

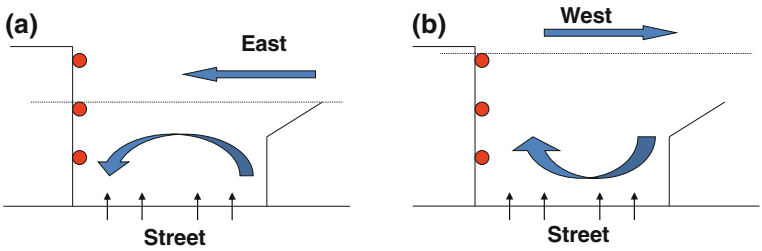

Fig. 10 Schematic flow patterns for **a** easterly and **b** westerly wind situations with measurement inlet points (*red*), separation lines and vortices that develop during wind situations

from traffic emissions along the street. The accumulated CO_2 was transported by the vortex towards the measurement inlet points, Figs. 8 and 10. In case of easterly wind, the CO_2 from the street was captured by the flow patterns in the low levels above the street and transported away from the measurement inlets by the counter-clockwise rotating eddies.

4 Conclusion

The results from the parametric study are in accordance with the recommendations for CFD calculations in urban areas [8,22]. The results show the ability of CFD to model complex flow patterns with highly heterogeneous geometry in very good agreement with high resolution temporal measurements in street canyons, where complex flow patterns can evolve. The evaluation with observation data leads to very good results for the mean velocity components within the complex study area. A strong dependency on the time-average periods of the Reynolds decomposition between the TKE values in a street canyon was found, which is an important aspect for comparing measurement data to RANS models results. Detailed analysis suggested that a time-average period of 15–60 s should be used for the Reynolds decomposition when comparing to RANS results in urban CFD calculations. This is similar

to the time-average periods used in other studies. The validation of the computed TKE values also led to good results, except in the detached flow regions at roof level.

This case-study demonstrates the usefulness of CFD methods in analyzing and simulating realistic flow patterns in urban areas based on a comparison with a dependent quantity (CO_2 concentration) that is a proxy for air pollution. The accuracy of the numerical approach to capture the CO_2 transport is shown by the comparison with the field data. Computation of the spatially distributed CO_2 concentrations led to a conclusive explanation for the strong dependency on the wind direction of measured CO_2 differences around a building. Completely different concentration profiles were found depending on the wind conditions in the street canyon. This shows that, in real urban areas, the concentration of pollutants can differ significantly from neighborhood scale and only detailed flow simulations combined with field measurements can give a detailed insight into the processes giving rise to complex urban flow patterns.

References

1. Andronopoulos S, Grigoriadis D, Robins A, Venetsanos A, Rafailidis S, Bartzis J (2002) Three-dimensional modelling of concentration fluctuations in complicated geometry. Environ Fluid Mech 1:415–440
2. ANSYS (2006) ANSYS CFX Reference Manual. ANSYS Inc., 11th edn
3. ANSYS (2006) ANSYS ICEM CFD Reference Manual. ANSYS Inc., 11th edn
4. Barlow J, Belcher S (2002) A wind tunnel model for quantifying fluxes in the urban boundary layer. Bound Layer Meteorol 104:131–150
5. Burrows DA, Hendricks EA, Diehl SR, Keith R (2007) Modeling turbulent flow in an urban central business district. J Appl Meteorol Climatol 46(12):2147–2164
6. Coirier W, Fricker D, Furmanczyk M, Kim S (2005) A computational fluid dynamics approach for urban area transport and dispersion modeling. Environ Fluid Mech 5:443–479
7. Davidson M, Snyder W, Lawson R Jr, Hunt J (1996) Wind tunnel simulations of plume dispersion through groups of obstacles. Atmos Environ 30(22):3715–3731
8. Franke J, Hirsch C, Jensen AG, Krüs HW, Schatzmann M, Westbury P, Miles S, Wisse J, Wright N (2004) Recommendations on the use of CFD in predicting pedestrian wind environment. In: COST Action C14. Impact of wind and storms on city life and built environment, Working group 2—CFD techniques
9. Grimmond C, King T, Cropley F, Nowak D, Souch C (2002) Local-scale fluxes of carbon dioxide in urban environments: methodological challenges and results from chicago. Environ Pollut 116:243–254
10. Hanna SR, Brown MJ, Camelli FE, Chan ST, Coirier WJ, Hansen OR, Huber AH, Kim S, Reynolds RM (2006) Detailed simulations of atmospheric flow and dispersion in downtown Manhatten—an application of five computational fluid dynamics models. Am Meteorol Soc, pp 1713–1726
11. Huang Y, Hu X, Zeng N (2009) Impact of wedge-shaped roofs on airflow and pollutant dispersion inside urban street canyons. Build Environ 44:2335–2347
12. Lee I, Park H (1994) Parameterization of the pollutant transport and dispersion in urban street canyons. Atmos Environ 28(14):2343–2349
13. Li X, Liu C, Leung D, Lam K (2006) Recent progress in CFD modelling of wind field and pollutant transport in street canyons. Atmos Environ 40:5640–5658
14. Lundquist J, Chan S (2006) Consequences ofurban stability conditions for computational fluid dynamics simulations of urban dispersion. J Appl Meteorol Climatol 46:1080–1097
15. Macdonald RW, Friffiths R, Hall D (1998) A comparison of results from scaled field and wind tunnel modelling of dispersion in arrays and obstacles. Atmos Environ 32(22):3845–3845
16. Menter F (1994) Two-equation eddy-viscosity turbulence models for engineering applications. AIAA J 32(8):1598–1605
17. Murena F, Favale G, Vardoulakis S, Solazzo E (2009) Modelling dispersion of traffic pollution in a deep street canyon: application of CFD and operational models. Atmos Environ 43:2303–2311
18. Pope SB (2000) Turbulent flows. Cambridge University Press,
19. Richards P, Hoxey R (1993) Appropriate boundary conditions for computational wind engineering models using the k-e turbulence model. J Wind Eng Ind Aerodyn 46(and 47):145–153
20. Rotach M, Vogt R, Bernhofer C, Batchvarova E, Christen A, Clappier A, Feddersen B, Gryning SE, Martucci G, Mayer H, Miteva V, Oke T, Parlow E, Richner H, Roth M, Roulet Y, Ruffieux D, Salmond

J, Schatzmann M, Voogt J (2005) Bubble—an urban boundary layer meteorology project. Theor Appl Climatol 81:231–261
21. Sini J, Anquetin S, Mestayer PG (1996) Pollutant dispersion and thermal effect in urban street canyons. Atmos Environ 30(15):2659–2677
22. Tominaga Y, Mochida A, Yoshie R, Kataoka H, Nozu T, Yoshikawa M, Shirasawa T (2008) Aij guidelines for practical applications of CFD to pedestrian wind environment around buildings. J Wind Eng Ind Aerodyn 96:1749–1761
23. Tsai M, Chen K (2004) Measurements and three-dimensional modeling of air pollutatns dispersion in an urban street caynon. Atmos Environ 38:5911–5924
24. Vardoulakis S, Fisher BE, Pericleous K, Gonzalez-Flesca B (2003) Modelling air quality in street canyons: a review. Atmos Environ 37:155–182
25. Versteeg H, Malalasekera W (2007) An introcudtion to computational fluid dynamics. 2. Pearson Education Limited,
26. Vogt R, Eitel J, Parlow E (2006) Coupling of backyard to street canyon CO_2 concentrations. In: 6th International conference on urban climate ICUC-6, Sweden
27. Wang X, McNamara K (2006) Evaluation of CFD simulation using RANS turbulence models for building effects on pollutant dispersion. Environ Fluid Mech 6:181–202
28. Weber S, Weber K (2008) Coupling of urban street canyon and backyard particle concentrations. Meteorol Z 17:251–261
29. Xie Z, Castro IP (2009) Large-eddy simulation for flow and dispersion in urban streets. Atmos Environ 43:2174–2185